THE JOURNAL OF PHYSICAL CHEMISTRY LETTERS
A JOURNAL OF THE AMERICAN CHEMICAL SOCIETY

pubs.acs.org/JPCL

Letter

Rational Design of Heteroanionic Two-Dimensional Materials with Emerging Topological, Magnetic, and Dielectric Properties

Yuhui Li, Yan-Fang Zhang, Jun Deng, Wen-Han Dong, Jia-Tao Sun, Jinbo Pan,* and Shixuan Du*

Cite This: *J. Phys. Chem. Lett.* 2022, 13, 3594−3601

Read Online

ACCESS | Metrics & More | Article Recommendations | Supporting Information

ABSTRACT: Designing and tuning the physical properties of two-dimensional (2D) materials at the atomic level are crucial to the development of 2D technologies. Here, we introduce heteroanions into metal-centered octahedral structural units of a 2D crystal breaking the O_h symmetry, together with the synergistic effect of anions' electrons and electronegativity, to realize ternary 2D materials with emerging topological, magnetic, and dielectric properties. Using an intrinsic heteroanionic van der Waals layered material, VOCl, as a prototype, 20 2D monolayers VXY (X = B, C, N, O, or F; Y = F, Cl, Br, or I) are obtained and investigated by means of first-principles calculations. The anion engineering in this family significantly reshapes the electronic properties of VOCl, leading to nonmagnetic topological insulators with nontrivial edge states in VCY, ferromagnetic half-semimetals with a nodal ring around the Fermi energy in VNY, and insulators with dielectric constants in VOY higher than that of *h*-BN. This work demonstrates the rationality and validity of the design strategy of multiple-anion engineering to achieve superior properties in the 2D monolayers with potential application in electronics and spintronics.

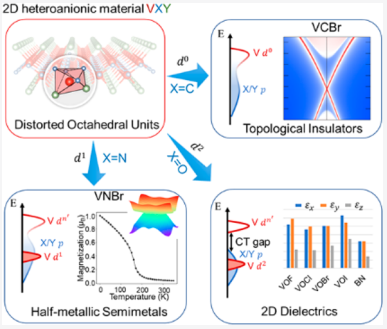

The past decade has witnessed great progress in the construction and characterization of two-dimensional (2D) materials. Thousands of 2D layered materials, which can be classified into tens of prototypes, were theoretically predicted by combining data-mining layered materials from traditional bulk materials databases and high-throughput computations.[1−4] These 2D databases provide efficient platforms for screening more 2D functional materials for the purpose of fabricating next-generation high-performance electronic,[5,6] optoelectronic,[7,8] and spintronic devices.[9,10] However, the discovery of 2D materials with the desired properties and superior performance is still challenging. For example, 2D materials with intrinsic magnetism, topological properties, and superior dielectric properties, which are important for state-of-the-art miniaturized applications in spintronics, quantum computing, and field-effect transistors, have rarely been reported in experiments or limited to several exemplary materials.[10−18]

Great efforts have been made to design and discover new 2D functional materials or to tune existing ones to exhibit the properties mentioned above. The methods used typically were chemical substitution[19,20] and the construction of heterostructures.[21,22] In transition metal compounds (TMCs), anion engineering is one very effective method, because the anions hybridize with metal cations and greatly influence the band gaps, band dispersions, crystal field splitting, etc.[23−25] Understanding how the variation of anions affects the electronic structures and physical properties is crucial for guiding the architecture of new functional 2D materials. For example, the band gap gradually decreases with anionic electronegativity in single-layer chromium trihalides CrX_3 (X = Cl, Br, or I), which makes $CrBr_3$ and CrI_3 possible candidates for optoelectronic applications.[19] The magnetic anisotropy due to spin−orbit coupling gradually increases with the atomic number of anions in monolayer CrX_3, leading to the robust Ising ferromagnetism in CrI_3.[26,27] In addition to homoanionic materials, some 2D heteroanionic compounds with multiple anions have been reported, in which the different anionic characteristics, such as charge, ionic radii, electronegativity, and polarizability, add new dimensions for controlling and tuning the physical properties of materials.[28,29]

In this work, we propose that desired magnetic, topological, and other properties can be artificially designed in heteroanionic 2D TMCs by fine-tuning electron occupation, ligand electronegativity, and crystal field strength. We first take the TMCs with metal-centered octahedral structural units as an example. The introduction of heteroanions distorts the original octahedral units, further splitting the d orbitals of transition metals. The band-filling, the d orbital splitting mode, including the splitting strength and orbital sequence, and p−d hybridization can be precisely modulated by a balance of anion electrons, electronegativity, and crystal field strength. This

Received: March 1, 2022
Accepted: April 13, 2022

https://doi.org/10.1021/acs.jpclett.2c00620
J. Phys. Chem. Lett. 2022, 13, 3594−3601

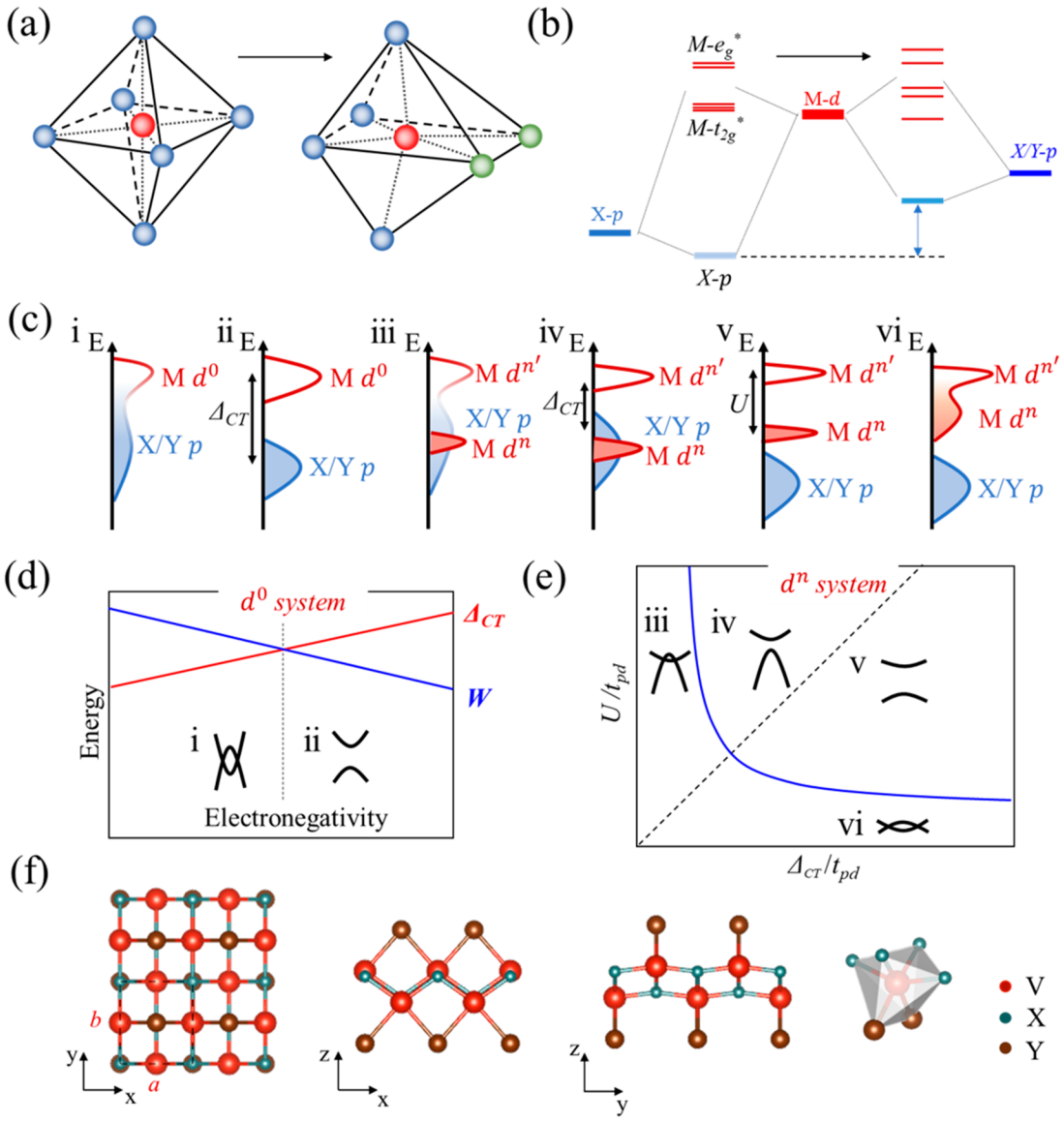

Figure 1. Design rule of electronic structure for heteroanion ternary compounds with octahedral motifs. (a) Reduction of local symmetry and (b) variation of orbital hybridization upon anion substitution. (c) Schematic variation of the density of states (DOS) for d^0 and d^n systems: (i) metal, (ii) semiconductor, (iii) p-type magnetic metal, (iv) charge-transfer semiconductor with a small hole effective mass and a large electron mass, (v) Mott−Hubbard insulator with large hole and electron masses, and (vi) d-band metal. (d and e) Schematic phase diagrams of electronic structures for d^0 and d^n systems corresponding to panel c. (f) Top and side views of the VXY monolayer and the distorted octahedra in VXY. The red, green, and brown spheres represent V, ligands X, and ligands Y, respectively.

results in highly diverse electronic and magnetic properties such as nonmagnetic metallicity, nonmagnetic semiconducting, magnetic charge-transfer semiconducting, magnetic Mott−Hubbard insulating, etc. We then choose monolayer VOCl as our anion engineering prototype structure by data-mining the 2D materials database.[2,3] The calculation results on VXY compounds (X = B, C, N, O, or F; Y = F, Cl, Br, or I) verify the feasibility of the multianion design strategy. The VCY compounds with d^0 cations are all semimetals with topological nontrivial edge states around the Fermi energy when considering spin−orbital coupling (SOC). The VNY with d^1 cations can be a ferromagnetic charge-transfer semiconductor or a half-metallic semimetal with a nodal ring around the Fermi energy. The VOY with d^2 cations can be a charge-transfer semiconductor or a Mott−Hubbard insulator with antiferromagnetism and high dielectric constants.

Design Approach for Heteroanionic 2D Materials. Most multicomponent crystals are constructed from metal−anion polyhedral units. Here, we mainly focus on 2D TMCs with octahedral units (left panel of Figure 1a). In this octahedral crystal unit, metal d orbitals hybridize with the surrounding ligand p orbitals, producing p-derived bonding states and d-derived antibonding states (left panel of Figure 1b). The five d orbitals will split into two sets of nondegenerate d orbitals, the higher double-degenerate e_g* orbitals that directly point toward the ligands forming stronger σ hybridization and lower 3-fold degenerate t_{2g}* orbitals with slightly weak π hybridization.[30] In previous reports, great effort has been devoted to modulating the d-band occupation and e_g*−t_{2g}* splitting strength by tuning the cations with different electrons and anions with different field strengths.[31,32] It is well-known that the electronic structure of a material is related to both the

https://doi.org/10.1021/acs.jpclett.2c00620
J. Phys. Chem. Lett. 2022, 13, 3594−3601

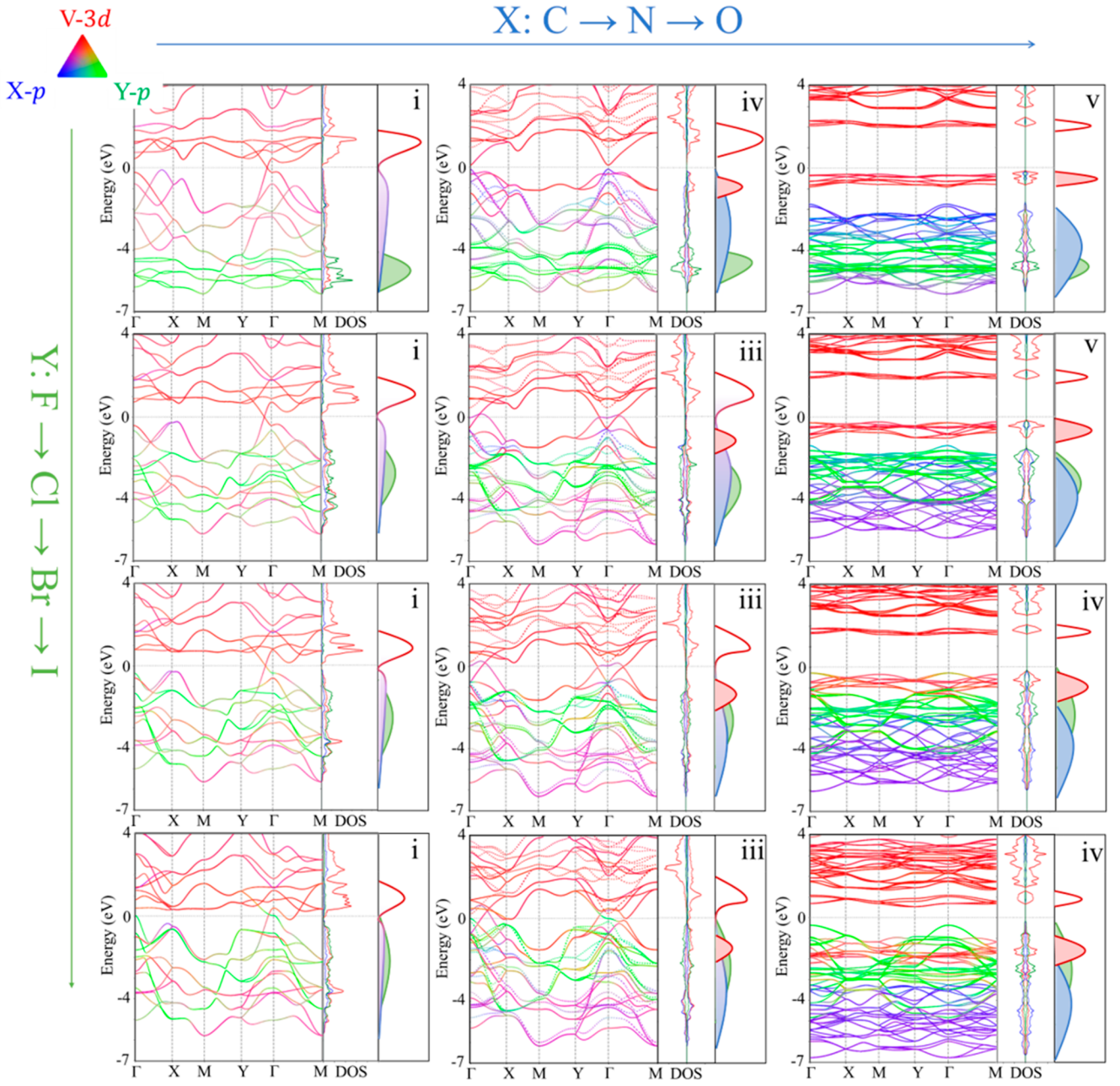

Figure 2. Orbital-projected band structures, DOS, and schematic DOS of VXY, in which X varies from carbon to oxygen and Y varies from fluorine to iodine. A color scheme is used to visualize the contribution of the atomic orbital to each band. The marked numbers in each panel correspond to the various situations shown in Figure 1b. Red, blue, and green colors represent the contributions from the V 3d orbitals, X 2p orbitals, and Y p orbitals, respectively. The solid lines and dashed lines represent the spin-up channel and spin-down channel, respectively.

local polyhedral symmetry and the global crystal symmetry. Even the d orbitals belonging to the same e_g* (or t_{2g}*) orbital may have different parities, and properties such as topological properties require fine control of orbital occupation and band edge positions.[33,34] However, this modulation is difficult to achieve in an intrinsic single anionic crystal with ideal octahedral units.

Reducing the local structure symmetry is a feasible solution for overcoming these challenges, because it results in further splitting of d orbitals (right panel of Figure 1b), as already demonstrated in materials under strain.[35,36] Substituting part of the anions in the octahedron with other anions is another solution for reducing the local symmetry (right panel of Figure 1a). The heteroanionic material design strategy is even more promising, where the heteroanions with different anionic characteristics, such as charge, ionic radii, electronegativity, and polarizability, add more tunable freedom. Therefore, the strategy may result in the superior performance of the material or even produce new properties that do not exist in single anionic crystals.[25,37]

According to the diverse antibonding d-band filling status, TMCs are classified into two categories, d^0 system (empty d-derived bands and partially or fully filled p-derived bands) and d^n system (partially filled d-derived bands and fully filled p-derived bands). For a d^0 system, an increase in the anion electronegativity leads to the enhancement of charge-transfer energy Δ_{CT} (red line in Figure 1d), which corresponds to the energy needed to transfer one p electron to an empty d-derived

https://doi.org/10.1021/acs.jpclett.2c00620
J. Phys. Chem. Lett. 2022, 13, 3594−3601

band.[30] At the same time, bandwidth W (blue line in Figure 1d) decreases due to the weakened d−p hybridization, which is proportional to the hopping interaction between anion p orbitals and metal d orbitals [t_{pd} (detailed discussion in Note S1)]. When the anion electronegativity is close to the metal electronegativity and bandwidth W is larger than charge-transfer gap Δ_{CT}, metallic or semimetallic properties can be obtained (region i in panels c and d of Figure 1). As the anion electronegativity exceeds a critical value, a metallic-insulating transition occurs, and the band gap gradually increases as the anion electronegativity increases (region ii in panels c and d of Figure 1). As for d^n TMCs, their rich electronic structures can be depicted within the Zaanen, Sawatzky, and Allen (ZSA) framework.[38] One of the important energy scales in d^n TMCs is on-site Coulomb energy U, which is the energy needed to accommodate an additional d electron from another metal site. Hence, on-site Coulomb energy U would lead to the localization of d electrons, producing local magnetic moments on the metal site. For a moderate U value, as the anion electronegativity increases, a p-type metal (region iii in panels c and e of Figure 1) would transform into a charge-transfer semiconductor (region iv in panels c and e of Figure 1). When the anion electronegativity exceeds a critical value, charge-transfer energy Δ_{CT} is larger than on-site Coulomb energy U, and a charge-transfer semiconductor then would transform into a Mott−Hubbard insulator (region v in panels c and e of Figure 1). Furthermore, if the U value decreased, a Mott−Hubbard insulator would transform into a d-band metal[39] (region vi in panels c and e of Figure 1). The change in the anionic combination in heteroanionic materials can affect the electron filling, p−d hydridization, sequence, and strength of d orbital splitting, thus inducing highly tunable and manifold properties of TMCs.

Structure and Stability of VXY Monolayers. By data-mining the 2D materials database,[2,3] we find that monolayer VOCl is a heteroanionic crystal with quasi-octahedral units. In addition, the V atom with a $3d^34s^2$ valence electronic configuration has extremely rich oxidation states, which is suitable for the production of both d^0 and d^n systems when coordinated by different anions. By substituting the anions with other anions, we obtain 20 monolayer vanadium-based compounds VXY (X = B, C, N, O, or F; Y = F, Cl, Br, or I). Figure 1f gives the geometric structure, showing that VXY crystallizes in the orthorhombic structure with a *Pmmn* space group. The middle VX layer is sandwiched by two halide layers. Each V atom is 6-fold coordinated with four X anions and two Y anions, leading to a strongly distorted octahedron unit with C_{2v} local symmetry.

The optimized lattice parameters of VXY are listed in Table S1. Lattice constant a increases with the size of the Y anion (from fluorine to iodine), while b is less affected because the halides are directly bonded to V atoms along the x-direction. Furthermore, we calculated their cohesive energies, formation energies (Table S1), phase diagrams (Figure S1), and phonon dispersions (Figure S2) to evaluate their thermodynamical and dynamical stabilities. We also performed *ab initio* molecular dynamics simulations (Figure S3) to evaluate the thermal stability of VXY monolayers at room temperature (300 K). Most of the VXY compounds show good thermodynamic, dynamic, and thermal stabilities.

Electronic and Magnetic Properties. The 20 VXY compounds (X = B, C, N, O, or F; Y = F, Cl, Br, or I), with the X atom varied along the same row in the period table, cover all post-main groups (IIIA group to VIIA group), which leads to a gradual increase in the electronegativity and p electrons of the X atom (from $2p^1$ to $2p^5$). The electronegativity of halide atoms Y, which possess the same valence electrons, gradually decreases as the atomic size increases from fluorine to iodine (Table S2).

Considering that VXY contains two anions per formula, there are in total six p-derived bonding bands allowing 12 electrons to occupy them. When X varies from boron to fluorine, the total number of valence electrons of VXY increases from 11 to 15. Therefore, both VBY and VCY are d^0 systems, while VNY, VOY, and VFY are d^1, d^2, and d^3 systems, respectively. As mentioned above, the VBY and VCY systems should be metals or semimetals due to the small difference in electronegativity between X (boron and carbon) and V, belonging to case i in Figure 1d, while for the d^n systems, the local magnetic moments in V atoms gradually increase as the X anion changes from N to O and F due to the localization of d electrons. The band gaps of the d^n systems are related to the energy level of p states of the anion with less electronegativity. The electronic structures and magnetic properties as shown in Figures S4−S7 and Figure 2 indeed verify the hypotheses presented above (calculation methods are provided in Note S2).

As presented in Figure 2 and Figure S6, the bands around the Fermi energy are contributed by V d orbitals (red), X p orbitals (blue), and Y p orbitals (green). When X is varied from carbon to oxygen, the contribution of X p orbitals to electronic bands (bule region) gradually moves away from the Fermi energy, leading to less overlap between X p orbitals and V d orbitals, as well as less band dispersion and a larger band gap. Meanwhile, when Y is varied from fluorine to iodine, the contribution of Y p orbitals to electronic bands (green region) gradually moves toward the Fermi energy, leading to a decrease in the band gap, and the transition from a Mott−Hubbard insulator to a charge-transfer semiconductor in VOY.

For these three magnetic systems, the spin density differences (Figure S7) indicate that their magnetisms mainly originate from the localized electrons in V atoms. The local magnetic moments on the V atom for VNY, VOY, and VFY are 1, 2, and 3 μ_B, respectively. In our defined coordinate systems (Figure 1f), the d electron alignments of VNY, VOY, and VFY are shown in Figure S7, which is consistent with the spin density differences. More detailed information about how to calculate the magnetic ground states can be found in Figure S8 and Table S3. We employ the Heisenberg Hamiltonian model to calculate the nearest (J_1), next-nearest (J_2), and third-nearest (J_3) neighbor exchange interactions (more details in Note S3). The corresponding magnetic parameters are summarized in Table S4. We find that the VNY compounds exhibit a ferromagnetic ground state, while the VOY and VFY compounds show an antiferromagnetic ground state. The Curie temperature of VNY and the Néel temperatures of VOF and VFY are evaluated by dynamic Monte Carlo simulations. The Curie temperature of VNY gradually increases as Y changes from fluorine to iodine, reaching the highest transition value of 217 K in VNI. While the Néel temperatures of VOY and VFY are all small, VFY compounds generally have transition values higher than those of VOY (Figure S9). As the benchmark of our Monte Carlo simulation, the Curie temperature of the experimentally studied CrSBr monolayer is also calculated. We obtain a value of ∼180 K (Figure S10), which approaches the experimental result.[40] The Curie

https://doi.org/10.1021/acs.jpclett.2c00620
J. Phys. Chem. Lett. 2022, 13, 3594−3601

temperature of monolayer VNI is higher than that of monolayer CrSBr, while that of VNBr is slightly lower (161 K).

Topological Dirac Semimetals in the VCY d^0 System. Further analysis of topological properties demonstrates that the VCY systems exhibit nontrivial topological properties. With VCBr as an example, the electronic band structures with and without considering SOC are shown in Figure 3a. Due to the anisotropic rectangular lattice, Dirac point Λ is located between Γ and Y, in the absence of SOC, which slightly deviates from the high-symmetry point.[41] When considering the SOC effect, the degeneracy of the Dirac points is removed, resulting in a band gap of 94 meV, which is available for achieving quantum spin Hall effects at room temperature.[42] Because VCBr has inversion symmetry, the Z_2 topological invariant can be calculated from the product of parities of all occupied states at four time-reversal-invariant-momentum (TRIM) points in the 2D Brillouin zone.[43,44] The product of the parities of all occupied states is −1 at the Γ point but 1 for the other points due to the band double degeneracy at high-symmetry points X, Y, and M. Therefore, VCBr is a 2D topological insulator with a Z_2 invariant $\nu = 1$. The nontrivial topological properties are also verified by the calculation of the Wannier center[45,46] (Figure 3b). Any arbitrary reference line would cross the evolution lines of the Wannier center in the $k_z = 0$ plane an odd number of times, which further indicates VCBr is a quantum spin Hall insulator. According to the bulk edge correspondence principle,[47,48] the nontrivial one-dimensional edge states protected by time inversion symmetry can be observed within the SOC gap, as shown in Figure 3c. Furthermore, the spin Hall conductance (SHC) was calculated using the Kubo formula,[49,50] which shows the quantum spin Hall plateau within the SOC gap (Figure S11). Upon comparison of calculated spin Berry curvature $\Omega^s(\vec{k})$ in the whole 2D Brillouin zone (Figure 3d), the main contribution to SHC comes from the Λ points.

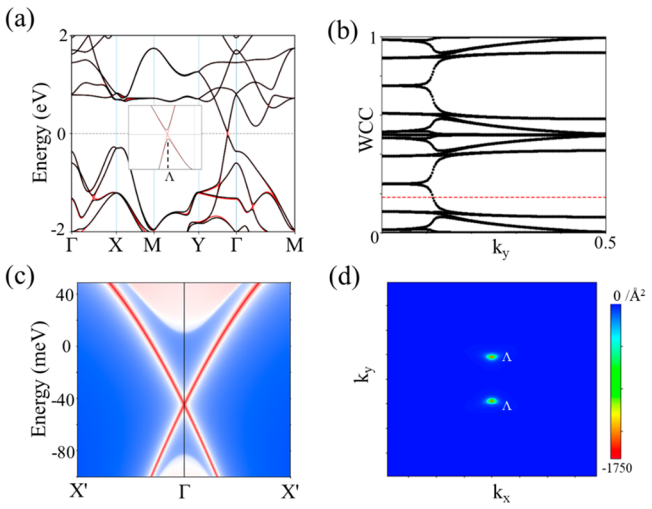

Figure 3. Topological properties of a VCBr monolayer. (a) Electronic band structure of VCBr, where black and red lines represent the band structures with and without SOC, respectively. The inset close-up shows the electronic structure along the Γ−Y high-symmetry line. (b) Evolution lines of Wannier centers for VCBr in the $k_z = 0$ plane. (c) Nontrivial topological edge states of VCBr. (d) Spin Berry curvatures for all occupied states in the 2D Brillouin zone.

Half-Metallic Semimetals in the VNY d^1 System. VNBr is a half-metallic semimetal with a 2D nodal loop near the Fermi level, where the electronic states are completely determined by a single spin component. The band structure in Figure 4a demonstrates that the monolayer VNBr has semimetallic character in the spin-up channel, while it has a semiconducting character with a band gap of 1.1 eV in the spin-down channel (Figure S12). The three-dimensional (3D) band structure (Figure 4b) indicates that the band intersection forms a closed nodal loop around the Γ point. By analyzing the structure symmetry of the VNBr monolayer, we found that the nodal loop is protected by nonsymmorphic glide mirror plane symmetry $g_z = \left\{M_z \middle| \frac{1}{2}\frac{1}{2}\right\}$. For $S = {}^1/_2$ particles, $g_z^2 = (-1)^{2S} = -1$. Hence, the eigenvalues of the g_z operator are $\pm i$. The g_z eigenvalues of two crossing bands are uncovered by plotting wave functions near the nodal loop (Figure S13). The wave functions from the red projected band that are mainly contributed by in-plane orbitals (Br p_x, N p_x, and V d_{xy}) are even under glide mirror plane operation. Instead, the wave functions of the other green projected band mainly composed of out-of-plane orbitals (N p_z and V d_{z^2}) are odd. The opposite g_z eigenvalues of the two crossing bands indicate that the gapless nodal loop is protected by glide mirror symmetry.[51,52] The magnetism of the VNBr monolayer is mainly due to the V atoms with a local magnetic moment of 1 μ_B per atom. The magnetic moment and magnetic susceptibility are mapped out as functions of temperature in Figure 4c, and the estimated Curie temperature of VNBr is 161 K. When considering magnetic anisotropic effects, the easy axis of magnetization is along the [100] direction, which is 32 and 211 μeV lower in energy than those along the [001] and [010] magnetization directions per unit cell, respectively. Figure 4d presents the band structure of VNBr with [100] magnetization. The nodal

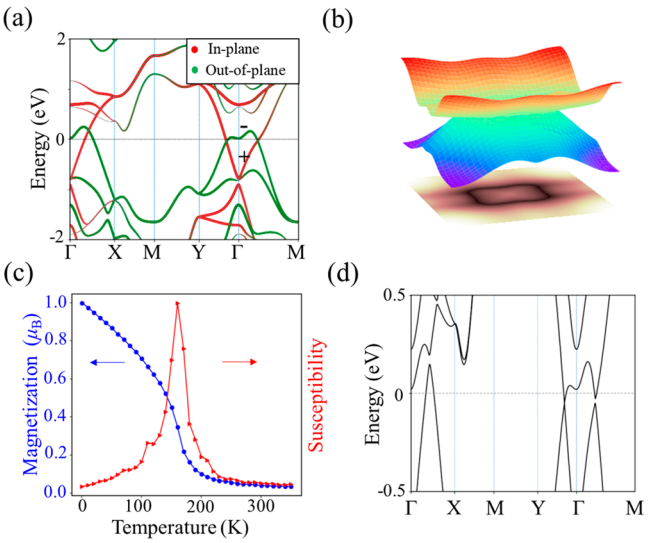

Figure 4. Electronic and magnetic properties of a VNBr monolayer. (a) Orbital-resolved band structure of VNBr in the spin-up channel, where green dots represent the contributions of out-of-plane orbitals (N p_z and V d_{z^2}) and red dots are composed of in-plane orbitals (Br p_x, N p_x, and V d_{xy}). (b) 3D band structures near the Fermi level in the spin-up channel. The projection at the bottom shows the nodal loop in 2D BZ. (c) Magnetization (blue dots) and susceptibility (red dots) of VNBr as a function of temperature. (d) Band structure of VNBr with [100] magnetization.

https://doi.org/10.1021/acs.jpclett.2c00620
J. Phys. Chem. Lett. 2022, 13, 3594−3601

Table 1. Macroscopic In-Plane and Out-Of-Plane Dielectric Constants of Monolayer and Bulk VOY, Compared with Those of *h*-BN

	bulk						monolayer					
	$\varepsilon_{x,\infty}$	$\varepsilon_{y,\infty}$	$\varepsilon_{z,\infty}$	$\varepsilon_{x,0}$	$\varepsilon_{y,0}$	$\varepsilon_{z,0}$	$\varepsilon_{x,\infty}$	$\varepsilon_{y,\infty}$	$\varepsilon_{z,\infty}$	$\varepsilon_{x,0}$	$\varepsilon_{y,0}$	$\varepsilon_{z,0}$
VOF	4.1	4.7	3.1	9.9	12.7	5.2	4.1	4.7	3.3	10.4	11.8	4.5
VOCl	4.7	4.3	3.6	9.1	9.7	4.4	4.7	4.3	3.7	9.2	9.9	4.3
VOBr	5.4	4.5	4.1	9.9	9.8	5.1	5.4	4.4	4.3	10.1	10.1	5.4
VOI	7.4	5.1	5.2	12.5	10.5	6.4	7.3	5.0	5.4	12.6	10.9	7.0
h-BN	4.7	4.7	2.6	6.5	6.5	3.0	4.7	4.7	2.5	6.4	6.4	2.8
h-BN[a]	4.98	4.98	3.03	6.93	6.93	3.76	4.97	4.97	2.89	6.82	6.82	3.29

[a]The data in this row are from ref 55.

loop is destroyed due to the vanishing glide mirror symmetry g_z under [100] magnetization. Only the crossing points on the Γ−Y high-symmetry line are preserved, which is protected by *x*-direction mirror symmetry M_x. The band structures with different magnetization directions are shown in Figure S14. When magnetization is along the [010] direction, the crossing points on the Γ−X high-symmetry line are preserved, which is protected by *y*-direction mirror symmetry M_y. For [110] magnetization, the whole nodal loop is destroyed. Instead, the nodal loop is robust against the SOC effect when VNBr possesses an out-of-plane spin-polarized direction.

Promising 2D Dielectrics in the VOY d^2 System. VOF and VOCl are Mott insulators with large band gaps, which is mainly due to on-site Coulomb repulsion energy *U* of 3d electrons at V atoms.[53] Figure S15 shows the effects of *U* on band structures in VOCl and VFCl. Upon exclusion of Coulomb repulsion, VOCl and VFCl are semiconductors with small band gaps that are determined by crystal field splitting. The inclusion of on-site Coulomb repulsion energy *U* would increase the difference in energy between the occupied states and unoccupied states, which largely increases the band gaps. To construct van der Waals (vdW) field-effect transistors (FETs), vdW dielectrics with high dielectric constants and large band gaps are needed. In fact, VOCl as the gate dielectric has been experimentally engineered in a graphene/VOCl/MoSe2 FET.[54] Therefore, we calculate the macroscopic in-plane and out-of-plane dielectric constants of VOY, as listed in Table 1. ε_0 is the static dielectric constant that includes both electronic and ionic contributions to the dielectric response, whereas optical dielectric constant ε_∞ contains only the electronic response. The static dielectric constants ε_0 are thus higher than the optical dielectric constants ε_∞. Due to the orthorhombic symmetry in VXY, the in-plane dielectric constants are anisotropic, where the electronic contribution to the *x*-direction dielectric constant ($\varepsilon_{x,\infty}$) is generally larger than that to the *y*-direction ($\varepsilon_{y,\infty}$) except for VOF, whereas the ionic contribution to the dielectric constant along the *y*-direction is larger than along the *x*-direction. In addition, the optical dielectric constants along the *x*-direction and *z*-direction gradually increase from VOF to VOI, whereas the *y*-direction optical dielectric constant is less affected. This is because the covalent composition between V atoms and Y atoms gradually increases as Y is varied from fluorine to iodine. Moreover, the differences in dielectric constants between the bulk and monolayer are small, indicating that the coupling between layers is weak. We also calculated the dielectric constants of *h*-BN for comparison and obtained results that are consistent with previous work.[55] The dielectric constants of VOY are much larger than those of *h*-BN, further suggesting that VOY compounds are promising 2D vdW gate dielectrics.

The Heyd−Scuseria−Ernzerhof screened hybrid functional (HSE06)[56] is also employed to check the reliability of the exotic properties of VXY. As one can see in Figure S16, the properties of all of the materials are robust at the HSE level. Furthermore, the interlayer coupling in VXY is very weak, as demonstrated in Figures S17 and S18. The band dispersions of the bulk VXY compounds are small along the *z*-direction, and the electronic bands around the Fermi energy in the *x*−*y* plane are almost unchanged, suggesting that the aforementioned properties can also be preserved in their multilayer or bulk forms. The calculated exfoliation energies show that these materials are easily exfoliated with exfoliation energies smaller than that of graphene.[57]

In summary, we have demonstrated the validity and rationality of a heteroanionic design strategy for guiding the search for new functional 2D TMCs in the future. As exemplary systems, most of the VXY compounds are predicted to be dynamically, thermodynamically, and thermally stable, and the emerging physical properties are effectively achieved as expected by tuning the anion ligands. Therein, nonmagnetic Dirac semimetals with nontrivial edge states, half-metallic semimetals with a nodal ring around the Fermi level, and insulators with superior dielectric properties were found in the VCY, VNY, and VOY systems, respectively. Beyond our studied VXY compounds, many other unexplored heteroanionic compounds await further exploration, e.g., MXY compounds with geometric structures similar to those of VXY,[58] Janus 2D materials,[29,59] anion-terminated MXenes,[60] etc. Our design strategy can be further applied to those systems, not only to largely enrich the current family of 2D materials but also to explain general trends over broad compositional spaces.

■ ASSOCIATED CONTENT

Supporting Information

The Supporting Information is available free of charge at https://pubs.acs.org/doi/10.1021/acs.jpclett.2c00620.

Hamiltonian of transition metal compounds; detailed calculation methods; structural, electronic, and magnetic properties of VXY; spin Hall plateau of VCBr; effect of Hubbard *U* on VOCl and VFCl; and exfoliation energy of VXBr (PDF)

■ AUTHOR INFORMATION

Corresponding Authors

Jinbo Pan − *Beijing National Laboratory for Condensed Matter Physics, Institute of Physics, Chinese Academy of Sciences, Beijing 100190, China; University of Chinese Academy of Sciences, Chinese Academy of Sciences, Beijing*

https://doi.org/10.1021/acs.jpclett.2c00620
J. Phys. Chem. Lett. 2022, 13, 3594−3601

100190, China; Songshan Lake Materials Laboratory, Dongguan 523808, China; Email: jbpan@iphy.ac.cn

Shixuan Du − *Beijing National Laboratory for Condensed Matter Physics, Institute of Physics, Chinese Academy of Sciences, Beijing 100190, China; University of Chinese Academy of Sciences, Chinese Academy of Sciences, Beijing 100190, China; Songshan Lake Materials Laboratory, Dongguan 523808, China; CAS Center for Excellence in Topological Quantum Computation, Beijing 100190, China;* orcid.org/0000-0001-9323-1307; Email: sxdu@iphy.ac.cn

Authors

Yuhui Li − *Beijing National Laboratory for Condensed Matter Physics, Institute of Physics, Chinese Academy of Sciences, Beijing 100190, China; University of Chinese Academy of Sciences, Chinese Academy of Sciences, Beijing 100190, China*

Yan-Fang Zhang − *University of Chinese Academy of Sciences, Chinese Academy of Sciences, Beijing 100190, China*

Jun Deng − *Beijing National Laboratory for Condensed Matter Physics, Institute of Physics, Chinese Academy of Sciences, Beijing 100190, China; University of Chinese Academy of Sciences, Chinese Academy of Sciences, Beijing 100190, China;* orcid.org/0000-0003-2420-8079

Wen-Han Dong − *Beijing National Laboratory for Condensed Matter Physics, Institute of Physics, Chinese Academy of Sciences, Beijing 100190, China; University of Chinese Academy of Sciences, Chinese Academy of Sciences, Beijing 100190, China*

Jia-Tao Sun − *School of Integrated Circuits and Electronics, MIIT Key Laboratory for Low-Dimensional Quantum Structure and Devices, Beijing Institute of Technology, Beijing 100081, China;* orcid.org/0000-0003-3519-352X

Complete contact information is available at: https://pubs.acs.org/10.1021/acs.jpclett.2c00620

Notes

The authors declare no competing financial interest.

■ ACKNOWLEDGMENTS

This work was supported by grants from the National Natural Science Foundation of China (61888102), the Major Program of the National Natural Science Foundation of China (92163206), the National Key Research and Development Program of China (2021YFA1201501), and the Strategic Priority Research Program of the Chinese Academy of Sciences (XDB30000000). Y.-F.Z. acknowledges the support of the National Natural Science Foundation of China (52102193) and the Fundamental Research Funds for the Central Universities. Computational resources were provided by the National Supercomputing Center in Tianjin.

■ REFERENCES

(1) Mounet, N.; Gibertini, M.; Schwaller, P.; Campi, D.; Merkys, A.; Marrazzo, A.; Sohier, T.; Castelli, I. E.; Cepellotti, A.; Pizzi, G.; et al. Two-Dimensional Materials from High-Throughput Computational Exfoliation of Experimentally Known Compounds. *Nat. Nanotechnol.* **2018**, *13*, 246−252.

(2) Haastrup, S.; Strange, M.; Pandey, M.; Deilmann, T.; Schmidt, P. S.; Hinsche, N. F.; Gjerding, M. N.; Torelli, D.; Larsen, P. M.; Riis-Jensen, A. C.; et al. The Computational 2D Materials Database: High-Throughput Modeling and Discovery of Atomically Thin Crystals. *2D Mater.* **2018**, *5*, 042002.

(3) Gjerding, M. N.; Taghizadeh, A.; Rasmussen, A.; Ali, S.; Bertoldo, F.; Deilmann, T.; Knøsgaard, N. R.; Kruse, M.; Larsen, A. H.; Manti, S.; et al. Recent Progress of the Computational 2D Materials Database (C2DB). *2D Mater.* **2021**, *8*, 044002.

(4) Curtarolo, S.; Hart, G. L.; Nardelli, M. B.; Mingo, N.; Sanvito, S.; Levy, O. The High-Throughput Highway to Computational Materials Design. *Nat. Mater.* **2013**, *12*, 191−201.

(5) Fiori, G.; Bonaccorso, F.; Iannaccone, G.; Palacios, T.; Neumaier, D.; Seabaugh, A.; Banerjee, S. K.; Colombo, L. Electronics Based on Two-Dimensional Materials. *Nat. Nanotechnol.* **2014**, *9*, 768−779.

(6) Chhowalla, M.; Jena, D.; Zhang, H. Two-Dimensional Semiconductors for Transistors. *Nat. Rev. Mater.* **2016**, *1*, 16052.

(7) Wang, Q. H.; Kalantar-Zadeh, K.; Kis, A.; Coleman, J. N.; Strano, M. S. Electronics and Optoelectronics of Two-Dimensional Transition Metal Dichalcogenides. *Nat. Nanotechnol.* **2012**, *7*, 699−712.

(8) Tian, H.; Chin, M. L.; Najmaei, S.; Guo, Q.; Xia, F.; Wang, H.; Dubey, M. Optoelectronic Devices Based on Two-Dimensional Transition Metal Dichalcogenides. *Nano Res.* **2016**, *9*, 1543−1560.

(9) Lin, X.; Yang, W.; Wang, K. L.; Zhao, W. Two-Dimensional Spintronics for Low-Power Electronics. *Nat. Electron.* **2019**, *2*, 274−283.

(10) Huang, B.; Clark, G.; Navarro-Moratalla, E.; Klein, D. R.; Cheng, R.; Seyler, K. L.; Zhong, D.; Schmidgall, E.; McGuire, M. A.; Cobden, D. H.; et al. Layer-Dependent Ferromagnetism in a Van Der Waals Crystal Down to the Monolayer Limit. *Nature* **2017**, *546*, 270−273.

(11) Fei, Z.; Palomaki, T.; Wu, S.; Zhao, W.; Cai, X.; Sun, B.; Nguyen, P.; Finney, J.; Xu, X.; Cobden, D. H. Edge Conduction in Monolayer WTe_2. *Nat. Phys.* **2017**, *13*, 677−682.

(12) Reis, F.; Li, G.; Dudy, L.; Bauernfeind, M.; Glass, S.; Hanke, W.; Thomale, R.; Schafer, J.; Claessen, R. Bismuthene on a SiC Substrate: A Candidate for a High-Temperature Quantum Spin Hall Material. *Science* **2017**, *357*, 287−290.

(13) Bonilla, M.; Kolekar, S.; Ma, Y.; Diaz, H. C.; Kalappattil, V.; Das, R.; Eggers, T.; Gutierrez, H. R.; Phan, M. H.; Batzill, M. Strong Room-Temperature Ferromagnetism in VSe_2 Monolayers on Van Der Waals Substrates. *Nat. Nanotechnol.* **2018**, *13*, 289−293.

(14) O'Hara, D. J.; Zhu, T.; Trout, A. H.; Ahmed, A. S.; Luo, Y. K.; Lee, C. H.; Brenner, M. R.; Rajan, S.; Gupta, J. A.; McComb, D. W.; et al. Room Temperature Intrinsic Ferromagnetism in Epitaxial Manganese Selenide Films in the Monolayer Limit. *Nano Lett.* **2018**, *18*, 3125−3131.

(15) Deng, Y.; Yu, Y.; Song, Y.; Zhang, J.; Wang, N. Z.; Sun, Z.; Yi, Y.; Wu, Y. Z.; Wu, S.; Zhu, J.; et al. Gate-Tunable Room-Temperature Ferromagnetism in Two-Dimensional Fe_3GeTe_2. *Nature* **2018**, *563*, 94−99.

(16) Gong, C.; Li, L.; Li, Z.; Ji, H.; Stern, A.; Xia, Y.; Cao, T.; Bao, W.; Wang, C.; Wang, Y.; et al. Discovery of Intrinsic Ferromagnetism in Two-Dimensional Van Der Waals Crystals. *Nature* **2017**, *546*, 265−269.

(17) Liu, Y.; Weiss, N. O.; Duan, X.; Cheng, H.-C.; Huang, Y.; Duan, X. Van Der Waals Heterostructures and Devices. *Nat. Rev. Mater.* **2016**, *1*, 16042.

(18) Li, T.; Tu, T.; Sun, Y.; Fu, H.; Yu, J.; Xing, L.; Wang, Z.; Wang, H.; Jia, R.; Wu, J.; et al. A Native Oxide High-K Gate Dielectric for Two-Dimensional Electronics. *Nat. Electron.* **2020**, *3*, 473−478.

(19) Zhang, W.-B.; Qu, Q.; Zhu, P.; Lam, C.-H. Robust Intrinsic Ferromagnetism and Half Semiconductivity in Stable Two-Dimensional Single-Layer Chromium Trihalides. *J. Mater. Chem. C* **2015**, *3*, 12457−12468.

(20) Zhang, H.; Liu, C.-X.; Qi, X.-L.; Dai, X.; Fang, Z.; Zhang, S.-C. Topological Insulators in Bi_2Se_3, Bi_2Te_3 and Sb_2Te_3 with a Single Dirac Cone on the Surface. *Nat. Phys.* **2009**, *5*, 438−442.

(21) Zhong, D.; Seyler, K. L.; Linpeng, X.; Cheng, R.; Sivadas, N.; Huang, B.; Schmidgall, E.; Taniguchi, T.; Watanabe, K.; McGuire, M. A.; et al. Van Der Waals Engineering of Ferromagnetic Semiconductor

Heterostructures for Spin and Valleytronics. *Sci. Adv.* **2017**, *3*, 1603113.
(22) Pan, J.; Yu, J.; Zhang, Y.-F.; Du, S.; Janotti, A.; Liu, C.-X.; Yan, Q. Quantum Anomalous Hall Effect in Two-Dimensional Magnetic Insulator Heterojunctions. *npj Comput. Mater.* **2020**, *6*, 152.
(23) Rao, C. N. R. Notable Effects of Aliovalent Anion Substitution on the Electronic Structure and Properties of Metal Oxides and Sulfides. *J. Phys. Chem. Lett.* **2015**, *6*, 3303−3308.
(24) Kouser, S.; Lingampalli, S. R.; Chithaiah, P.; Roy, A.; Saha, S.; Waghmare, U. V.; Rao, C. N. Extraordinary Changes in the Electronic Structure and Properties of CdS and ZnS by Anionic Substitution: Cosubstitution of P and Cl in Place of S. *Angew. Chem., Int. Ed.* **2015**, *54*, 8149−53.
(25) Harada, J. K.; Charles, N.; Poeppelmeier, K. R.; Rondinelli, J. M. Heteroanionic Materials by Design: Progress toward Targeted Properties. *Adv. Mater.* **2019**, *31*, 1805295.
(26) Xu, C.; Feng, J.; Xiang, H.; Bellaiche, L. Interplay between Kitaev Interaction and Single Ion Anisotropy in Ferromagnetic CrI_3 and $CrGeTe_3$ Monolayers. *npj Comput. Mater.* **2018**, *4*, 57.
(27) Kim, H. H.; Yang, B.; Li, S.; Jiang, S.; Jin, C.; Tao, Z.; Nichols, G.; Sfigakis, F.; Zhong, S.; Li, C.; et al. Evolution of Interlayer and Intralayer Magnetism in Three Atomically Thin Chromium Trihalides. *Proc. Natl. Acad. Sci. U. S. A.* **2019**, *116*, 11131−11136.
(28) Rajan, A. C.; Mishra, A.; Satsangi, S.; Vaish, R.; Mizuseki, H.; Lee, K.-R.; Singh, A. K. Machine-Learning-Assisted Accurate Band Gap Predictions of Functionalized MXene. *Chem. Mater.* **2018**, *30*, 4031−4038.
(29) Li, R.; Cheng, Y.; Huang, W. Recent Progress of Janus 2D Transition Metal Chalcogenides: From Theory to Experiments. *Small* **2018**, *14*, 1802091.
(30) Ushakov, A. V.; Streltsov, S. V.; Khomskii, D. I. Crystal Field Splitting in Correlated Systems with Negative Charge-Transfer Gap. *J. Phys.: Condens. Matter* **2011**, *23*, 445601.
(31) Chen, Q.; Ding, Q.; Wang, Y.; Xu, Y.; Wang, J. Electronic and Magnetic Properties of a Two-Dimensional Transition Metal Phosphorous Chalcogenide $TMPS_4$. *J. Phys. Chem. C* **2020**, *124*, 12075−12080.
(32) Pasquier, D.; Yazyev, O. V. Crystal Field, Ligand Field, and Interorbital Effects in Two-Dimensional Transition Metal Dichalcogenides across the Periodic Table. *2D Mater.* **2019**, *6*, 025015.
(33) Choe, D.-H.; Sung, H.-J.; Chang, K. J. Understanding Topological Phase Transition in Monolayer Transition Metal Dichalcogenides. *Phys. Rev. B* **2016**, *93*, 125109.
(34) Khazaei, M.; Ranjbar, A.; Arai, M.; Yunoki, S. Topological Insulators in the Ordered Double Transition Metals $M_2'M''C_2$ MXenes (M′ = Mo, W; M″ = Ti, Zr, Hf). *Phys. Rev. B* **2016**, *94*, 125152.
(35) Pinho, P. V. B.; Chartier, A.; Miserque, F.; Menut, D.; Moussy, J.-B. Impact of Epitaxial Strain on Crystal Field Splitting of A-Cr_2O_3(0001) Thin Films Quantified by X-Ray Photoemission Spectroscopy. *Mater. Res. Lett.* **2021**, *9*, 163−168.
(36) Ochi, M.; Arita, R.; Trivedi, N.; Okamoto, S. Strain-Induced Topological Transition In $SrRu_2O_6$ and $CaOs_2O_6$. *Phys. Rev. B* **2016**, *93*, 195149.
(37) Kageyama, H.; Hayashi, K.; Maeda, K.; Attfield, J. P.; Hiroi, Z.; Rondinelli, J. M.; Poeppelmeier, K. R. Expanding Frontiers in Materials Chemistry and Physics with Multiple Anions. *Nat. Commun.* **2018**, *9*, 772.
(38) Zaanen, J.; Sawatzky, G. A.; Allen, J. W. Band Gaps and Electronic Structure of Transition-Metal Compounds. *Phys. Rev. Lett.* **1985**, *55*, 418−421.
(39) Imada, M.; Fujimori, A.; Tokura, Y. Metal-Insulator Transitions. *Rev. Mod. Phys.* **1998**, *70*, 1039−1263.
(40) Lee, K.; Dismukes, A. H.; Telford, E. J.; Wiscons, R. A.; Wang, J.; Xu, X.; Nuckolls, C.; Dean, C. R.; Roy, X.; Zhu, X. Magnetic Order and Symmetry in the 2D Semiconductor CrSBr. *Nano Lett.* **2021**, *21*, 3511−3517.
(41) Dong, W.-H.; Bao, D.-L.; Sun, J.-T.; Liu, F.; Du, S. Manipulation of Dirac Fermions in Nanochain-Structured Graphene. *Chin. Phys. Lett.* **2021**, *38*, 097101.
(42) Kane, C. L.; Mele, E. J. Quantum Spin Hall Effect in Graphene. *Phys. Rev. Lett.* **2005**, *95*, 226801.
(43) Kane, C. L.; Mele, E. J. Z2 Topological Order and the Quantum Spin Hall Effect. *Phys. Rev. Lett.* **2005**, *95*, 146802.
(44) Fu, L.; Kane, C. L. Topological Insulators with Inversion Symmetry. *Phys. Rev. B* **2007**, *76*, 045302.
(45) Yu, R.; Qi, X. L.; Bernevig, A.; Fang, Z.; Dai, X. Equivalent Expression of Z2 Topological Invariant for Band Insulators Using the Non-Abelian Berry Connection. *Phys. Rev. B* **2011**, *84*, 075119.
(46) Soluyanov, A. A.; Vanderbilt, D. Computing Topological Invariants without Inversion Symmetry. *Phys. Rev. B* **2011**, *83*, 235401.
(47) Hsieh, D.; Qian, D.; Wray, L.; Xia, Y.; Hor, Y. S.; Cava, R. J.; Hasan, M. Z. A Topological Dirac Insulator in a Quantum Spin Hall Phase. *Nature* **2008**, *452*, 970−974.
(48) Hasan, M. Z.; Kane, C. L. Colloquium: Topological Insulators. *Rev. Mod. Phys.* **2010**, *82*, 3045−3067.
(49) Yao, Y.; Kleinman, L.; MacDonald, A. H.; Sinova, J.; Jungwirth, T.; Wang, D. S.; Wang, E.; Niu, Q. First Principles Calculation of Anomalous Hall Conductivity in Ferromagnetic Bcc Fe. *Phys. Rev. Lett.* **2004**, *92*, 037204.
(50) Yao, Y.; Fang, Z. Sign Changes of Intrinsic Spin Hall Effect in Semiconductors and Simple Metals: First-Principles Calculations. *Phys. Rev. Lett.* **2005**, *95*, 156601.
(51) Hu, Y.; Li, S. S.; Ji, W. X.; Zhang, C. W.; Ding, M.; Wang, P. J.; Yan, S. S. Glide Mirror Plane Protected Nodal-Loop in an Anisotropic Half-Metallic MnNF Monolayer. *J. Phys. Chem. Lett.* **2020**, *11*, 485−491.
(52) Fang, C.; Weng, H.; Dai, X.; Fang, Z. Topological Nodal Line Semimetals. *Chin. Phys. B* **2016**, *25*, 117106.
(53) Glawion, S.; Scholz, M. R.; Zhang, Y. Z.; Valentí, R.; Saha-Dasgupta, T.; Klemm, M.; Hemberger, J.; Horn, S.; Sing, M.; Claessen, R. Electronic Structure of the Two-Dimensional Heisenberg Antiferromagnet VOCl: A Multiorbital Mott Insulator. *Phys. Rev. B* **2009**, *80*, 155119.
(54) Zhu, W.; Cui, Q.; Adam, M. L.; Liu, Z.; Zhang, L.; Dai, Z.; Yin, Y.; Chen, S.; Song, L. Ternary VOCl Single-Crystal as Efficient Gate Dielectric for 2D Field-Effect Transistors. *2D Mater.* **2021**, *8*, 025010.
(55) Laturia, A.; Van de Put, M. L.; Vandenberghe, W. G. Dielectric Properties of Hexagonal Boron Nitride and Transition Metal Dichalcogenides: From Monolayer to Bulk. *npj 2D Mater. Appl.* **2018**, *2*, 6.
(56) Heyd, J.; Scuseria, G. E.; Ernzerhof, M. Hybrid Functionals Based on a Screened Coulomb Potential. *J. Chem. Phys.* **2003**, *118*, 8207−8215.
(57) Zacharia, R.; Ulbricht, H.; Hertel, T. Interlayer Cohesive Energy of Graphite from Thermal Desorption of Polyaromatic Hydrocarbons. *Phys. Rev. B* **2004**, *69*, 155406.
(58) Song, Y.; Pan, J.; Zhang, Y. F.; Yang, H.; Du, S. Monolayer Iridium Sulfide Halides with High Mobility Transport Anisotropy and Highly Efficient Light Harvesting. *J. Phys. Chem. Lett.* **2021**, *12*, 6007−6013.
(59) Chen, W.; Hou, X.; Shi, X.; Pan, H. Two-Dimensional Janus Transition Metal Oxides and Chalcogenides: Multifunctional Properties for Photocatalysts, Electronics, and Energy Conversion. *ACS Appl. Mater. Interfaces* **2018**, *10*, 35289−35295.
(60) Dong, L.; Kumar, H.; Anasori, B.; Gogotsi, Y.; Shenoy, V. B. Rational Design of Two-Dimensional Metallic and Semiconducting Spintronic Materials Based on Ordered Double-Transition-Metal MXenes. *J. Phys. Chem. Lett.* **2017**, *8*, 422−428.

https://doi.org/10.1021/acs.jpclett.2c00620
J. Phys. Chem. Lett. 2022, 13, 3594−3601